Journal of Advanced Ceramics
2021, **10**(1): 62–77
https://doi.org/10.1007/s40145-020-0417-2
ISSN 2226-4108
CN 10-1154/TQ

Research Article

One-step synthesis and electromagnetic absorption properties of high entropy rare earth hexaborides (HE REB_6) and high entropy rare earth hexaborides/borates (HE REB_6/HE $REBO_3$) composite powders

Weiming ZHANG[a], Biao ZHAO[b], Huimin XIANG[a], Fu-Zhi DAI[a], Shijiang WU[c], Yanchun ZHOU[a,*]

[a]*Science and Technology on Advanced Functional Composite Laboratory, Aerospace Research Institute of Materials & Processing Technology, Beijing 100076, China*
[b]*Henan Key Laboratory of Aeronautical Materials and Application Technology, School of Material Science and Engineering, Zhengzhou University of Aeronautics, Zhengzhou 450046, China*
[c]*Zibo Firststar New Material Incorporated Co., Ltd., Zibo 255000, China*

Received: July 29, 2020; Revised: August 23, 2020; Accepted: August 30, 2020

Abstract: Considering the emergence of severe electromagnetic interference problems, it is vital to develop electromagnetic (EM) wave absorbing materials with high dielectric, magnetic loss and optimized impedance matching. However, realizing the synergistic dielectric and magnetic losses in a single phase material is still a challenge. Herein, high entropy (HE) rare earth hexaborides (REB_6) powders with coupling of dielectric and magnetic losses were designed and successfully synthesized through a facial one-step boron carbide reduction method, and the effects of high entropy borates intermedia phases on the EM wave absorption properties were investigated. Five HE REB_6 ceramics including $(Ce_{0.2}Y_{0.2}Sm_{0.2}Er_{0.2}Yb_{0.2})B_6$, $(Ce_{0.2}Eu_{0.2}Sm_{0.2}Er_{0.2}Yb_{0.2})B_6$, $(Ce_{0.2}Y_{0.2}Eu_{0.2}Er_{0.2}Yb_{0.2})B_6$, $(Ce_{0.2}Y_{0.2}Sm_{0.2}Eu_{0.2}Yb_{0.2})B_6$, and $(Nd_{0.2}Y_{0.2}Sm_{0.2}Eu_{0.2}Yb_{0.2})B_6$ possess CsCl-type cubic crystal structure, and their theoretical densities range from 4.84 to 5.25 g/cm^3. $(Ce_{0.2}Y_{0.2}Sm_{0.2}Er_{0.2}Yb_{0.2})B_6$ powders with the average particle size of 1.86 μm were found to possess the best EM wave absorption properties among these hexaborides. The RL_{min} value of $(Ce_{0.2}Y_{0.2}Sm_{0.2}Er_{0.2}Yb_{0.2})B_6$ reaches –33.4 dB at 11.5 GHz at thickness of 2 mm; meanwhile, the optimized effective absorption bandwidth (E_{AB}) is 3.9 GHz from 13.6 to 17.5 GHz with a thickness of 1.5 mm. The introduction of HE $REBO_3$ (RE = Ce, Y, Sm, Eu, Er, Yb) as intermediate phase will give rise to the mismatching impedance, which will further lead to the reduction of reflection loss. Intriguingly, the HEREB_6/HE$REBO_3$ still possess wide effective absorption bandwidth of 4.1 GHz with the relative low thickness of 1.7 mm. Considering the better stability, low density, and good EM wave absorption properties, HE REB_6 ceramics are promising as a new type of EM wave absorbing materials.

Keywords: high entropy rare earth hexaborides (HE REB_6); one-step synthesis; electromagnetic wave absorbing properties; synergistic dielectric and magnetic losses; wide effective absorption bandwidth

* Corresponding author.
E-mail: yczhou@alum.imr.ac.cn

1 Introduction

With the electromagnetic (EM) wave as an important carrier of information exchange penetrating into all aspects in human life, it is critical to develop high performance EM wave absorbing materials to eliminate the adverse effects of EM wave, such as the electromagnetic interference and microwave pollution [1–3]. Under increasingly complex serving environment, EM wave absorbing materials are required to possess the following properties: (1) strong absorption, broad efficient absorption bandwidth, and optimized impedance matching; (2) lightweight, good mechanical property, and favorable high-temperature stability; (3) resistance to corrosion and oxidation; (4) easy fabrication and cost-efficient [3–5]. However, achieving high EM wave absorption performance with foregoing features in a single phase material is still a challenge [6]. For examples, magnetite with superior dual electromagnetic properties (ferrimagnetic and dielectric properties) has shortcomings of high density and inferior stability [7,8]; magnetic metals with high permeability have disadvantages of high density and poor resistance to environment corrosion [9,10]; lightweight carbon-based nanomaterials and conducting polymers both take the advantage of high conductivity but also suffer from dissatisfactory electromagnetic impedance matching [11–13]. Through element doping [14], structure design [15], surface treatment [10], and composite construction [16], weight reduction and impedance matching adjustment can be effectively realized. However, realizing synergistic dielectric and magnetic losses in a single phase material is still difficult. Thus, searching for materials with good high-temperature stability, corrosion and oxidation resistance is appealing. Consequently, it is of great significance to develop lightweight high temperature EM wave absorbing ceramics with exceptional corrosion and oxidation resistance.

EM wave absorbing materials are capable of converting absorbed EM wave into thermal energy in terms of dielectric loss and/or magnetic loss [17]. Considering the conductivity and magnetism of rare-earth (RE) hexaborides (REB_6), it is expected that lightweight REB_6 ceramics possess promising EM wave absorption properties. REB_6 exhibits a CsCl-type crystal structure, with an RE atom surrounded by eight boron octahedra [18]. The boron framework is deficient of 2 electrons that can be donated by RE atoms, making divalent REB_6 (EuB_6, YbB_6) semiconductors or semimetals while other trivalent REB_6 conductors [19–22]. Besides, the rigidity of octahedral boron cage endows REB_6 with high melting point, high hardness in lattice *a* direction, and superior chemical stability [23,24]. The substitution of RE atoms leads to the adjustment of the distances of intra-octahedron bond ($B–B_{intra}$) and inter-octahedra bond ($B–B_{inter}$), which will affect the electrical properties and then give rise to the transition of conductivity from semiconductors to conductors [25,26]. It is also found that with the exception of paramagnetic LaB_6, trivalent REB_6 are antiferromagnetic at low temperature and EuB_6 exhibits unusual ferromagnetism below 15.3 K [27–31]. Surprisingly, $(Ca_{1-x}La_x)B_6$ has a ferromagnetic Curie temperature of 600 K, which equals to that of transition-metal ferromagnets such as Fe [32]. Combining excellent high-temperature property, good electrical conductivity and magnetic property, REB_6 are expected to be a new type of promising EM wave absorbing materials.

The similar lattice parameters of different REB_6 is beneficial to tuning the properties of REB_6 through element doping [26,33]. Besides, boron carbide reduction method is found effective to synthesize REB_6 without post-synthesis treatment such as acid washing [34,35]. Consequently, it is feasible to design and synthesize high-entropy rare-earth hexaborides (HE REB_6) with multi-principal rare-earth elements. It is expected that the introduction of configuration entropy can yield a batch of unexpected properties including better resistance to environment attack, better oxidation and corrosion resistance, good high-temperature stability, and lower thermal conductivity [36–42]. Most importantly, the "cocktail" effect on electrical and magnetic properties is anticipated which will open a new door to tailor EM wave absorbing properties including absorbing capability, effective absorbing bandwidth, and impedance matching. Previous work in the authors' lab has found that high-entropy rare-earth silicide carbide/rare-earth oxide composites show a wide efficient absorption bandwidth of 4.5 GHz with a maximum reflection loss of –50.9 dB at thickness of 2.0 mm [43]. However, by far EM wave absorption properties of HE REB_6 have not been explored.

The aims of this work are to design and synthesize HE REB_6 and to explore the EM wave absorption properties of HE REB_6. To achieve these goals, five high-entropy rare-earth hexaborides $(Ce_{0.2}Y_{0.2}Sm_{0.2}Er_{0.2}Yb_{0.2})B_6$, $(Ce_{0.2}Eu_{0.2}Sm_{0.2}Er_{0.2}Yb_{0.2})B_6$, $(Ce_{0.2}Y_{0.2}Eu_{0.2}Er_{0.2}Yb_{0.2})B_6$, $(Ce_{0.2}Y_{0.2}Sm_{0.2}Eu_{0.2}Yb_{0.2})B_6$, and $(Nd_{0.2}Y_{0.2}Sm_{0.2}Eu_{0.2}$

$Yb_{0.2})B_6$ are designed and successfully synthesized. Hereafter they are referred to as HE REB_6-1, HE REB_6-2, HE REB_6-3, HE REB_6-4, and HE REB_6-5. The choice of rare-earth elements is due to the following considerations. Firstly, hexaborides containing these RE elements exhibit the same crystal structure. Secondly, as shown in Table 1 [44], the difference of selected ion radius is smaller than 15%, which makes the formation of solid solution with a single phase easy. Thirdly, the selected compounds including NdB_6, SmB_6, YB_6, ErB_6, and CeB_6 are conductors with antiferromagnetism, while EuB_6 is a semiconductor with two ferromagnetic transition temperature of 12.5 and 15.3 K. Fourthly, although some REB_6 such as YbB_6 is a semiconductor, the formation of high-entropy hexaborides could lead to the band gap narrowing which can tune the electrical conductivity [45]. The electrical conductivity and magnetic ordering in hexaborides endow these new types of HE REB_6 promising EM wave absorption properties. Finally, the selected compounds also take advantages of lightweight, exceptional high-temperature stability, and favorable resistant to corrosion and oxidation. The formation of HE REB_6 could lead to further improvement of the comprehensive properties including mechanical property, thermal property, and EM wave absorption property.

2 Experimental

2. 1 Synthesis of HE REB_6 powders

Five HE REB_6, i.e., $(Ce_{0.2}Y_{0.2}Sm_{0.2}Er_{0.2}Yb_{0.2})B_6$, $(Ce_{0.2}Eu_{0.2}Sm_{0.2}Er_{0.2}Yb_{0.2})B_6$, $(Ce_{0.2}Y_{0.2}Eu_{0.2}Er_{0.2}Yb_{0.2})B_6$, $(Ce_{0.2}Y_{0.2}Sm_{0.2}Eu_{0.2}Yb_{0.2})B_6$, and $(Nd_{0.2}Y_{0.2}Sm_{0.2}Eu_{0.2}Yb_{0.2})B_6$ powders were synthesized by a one-step boron carbide reduction process using commercially available Y_2O_3, CeO_2, Sm_2O_3, Eu_2O_3, Er_2O_3, Yb_2O_3 powders (99.9% purity, 1 μm, HWRK Chem Co., Ltd., Beijing, China) and B_4C powders (98% purity, –200 mesh, Mudanjiang Qianjin Reagent Co. Ltd., Heilongjiang, China) as starting materials. Five rare earth oxide powders in the stoichiometric ratio of required HE REB_6 were mixed together with B_4C powders to prepare HE REB_6 powders. The initial stage of the boron carbide reduction process leads to the formation of $REBO_3$ as an intermediate phase as described by Eqs. (1)–(4), where RE refers to Y, Sm, Eu, Er, or Yb. In particular, the molar ratio of reactants is listed in Table 2.

$$4RE_2O_3 + 7B_4C = 4REBO_3 + REB_6 + 7C \quad (1)$$

$$4REBO_3 + 7C + 5B_4C = 4REB_6 + 12CO \quad (2)$$

$$6CeO_2 + 4B_4C = 4CeBO_3 + 2CeB_6 + 4C \quad (3)$$

$$4CeBO_3 + 4C + 5B_4C = 4CeB_6 + 9CO + \frac{3}{2}O_2 \quad (4)$$

Each mixture was ball-milled with ethanol and agate media in a polytetrafluoroethylene jar for 4 h. After ball milling, the homogeneously mixed slurry was fully dried in an oven at 60 ℃. After drying and being sieved through a 120-mesh screen, the mixed powders were uniaxially cold-pressed into cylindrical pellets of 30 mm diameter in a stainless-steel die. Eventually, the green bodies were heated to 1900 ℃ and held for 1 h in vacuum to synthesize pure HE REB_6 powders. In order to study the influence of intermediate phases, i.e., high-entropy rare-earth borates (HE $REBO_3$) on the EM wave absorption performance of HE REB_6, the pellets were heated to 1600 ℃ and kept for 1 h in Ar atmosphere to obtain HE REB_6/HE $REBO_3$ composites. The as-prepared samples were ground into powders in an agate mortar for subsequent characterizations.

Table 1 Ion radius and radius difference of the selected RE ions for the design of HE REB_6 (data were obtained from the revised list of effective ionic radii [44])

RE	Ion radius (Å)	Radius difference (%)
Nd	0.98	11
Sm	0.96	9
Eu	0.95	8
Y	0.90	3
Er	0.89	2
Ce	0.87	0
Yb	0.87	0

Table 2 Constituent of raw materials of HE REB_6

HE compound	Molar ratio of raw materials
$(Ce_{0.2}Y_{0.2}Sm_{0.2}Er_{0.2}Yb_{0.2})B_6$	2 CeO_2 : 1 Y_2O_3 : 1 Sm_2O_3 : 1 Er_2O_3 : 1 Yb_2O_3 : 15 B_4C
$(Ce_{0.2}Eu_{0.2}Sm_{0.2}Er_{0.2}Yb_{0.2})B_6$	2 CeO_2 : 1 Eu_2O_3 : 1 Sm_2O_3 : 1 Er_2O_3 : 1 Yb_2O_3 : 15 B_4C
$(Ce_{0.2}Y_{0.2}Eu_{0.2}Er_{0.2}Yb_{0.2})B_6$	2 CeO_2 : 1 Y_2O_3 : 1 Eu_2O_3 : 1 Er_2O_3 : 1 Yb_2O_3 : 15 B_4C
$(Ce_{0.2}Y_{0.2}Sm_{0.2}Eu_{0.2}Yb_{0.2})B_6$	2 CeO_2 : 1 Y_2O_3 : 1 Sm_2O_3 : 1 Eu_2O_3 : 1 Yb_2O_3 : 15 B_4C
$(Nd_{0.2}Y_{0.2}Sm_{0.2}Eu_{0.2}Yb_{0.2})B_6$	1 Nd_2O_3 : 1 Y_2O_3 : 1 Sm_2O_3 : 1 Eu_2O_3 : 1 Yb_2O_3 : 15 B_4C

2. 2 Phase composition, microstructure, and EM absorbing properties

Phase composition was analyzed by an X-ray diffractometer (XRD, D8 Advanced, Bruker, Germany) utilizing Cu Kα radiation (λ = 1.5406 Å) with a step size of 0.02° at a scanning rate of 2 (°)/min. The weight fraction of intermediate phase is quantitatively analyzed using the total pattern solution software (TOPAS, Bruker Corp., Karlsruhe, Germany). The microstructure of as-prepared HE REB_6 powders was investigated by a scanning electron microscope (SEM, Apollo 300, CamScan, UK) equipped with an energy dispersive spectroscopy system (EDS Inca X-Max 80 T, Oxford, UK).

The relative complex permeability ($\mu_r = \mu' + j\mu''$) and permittivity ($\varepsilon_r = \varepsilon' + j\varepsilon''$) were determined by a vector network analyzer (Agilent N5244A, USA) using the coaxial method in the frequency range of 1.0–18.0 GHz. High-entropy REB_6 powders and paraffin wax were mixed at a mass ratio of 7:3 and compacted into a toroidal shape (Φ_{out} = 7.00 mm, Φ_{in} = 3.04 mm). The reflection loss (*RL*), which is one of the evaluation criteria for the EM wave absorption properties, was determined from the relative complex permeability and permittivity for a given frequency and absorber thickness based on the transmission-line theory and metal back-panel model [46], according to Eqs. (5) and (6):

$$RL(\mathrm{dB}) = 20\log\left|(Z_{in} - Z_0)/(Z_{in} + Z_0)\right| \quad (5)$$

$$Z_{in} = Z_0\sqrt{\frac{\mu_r}{\varepsilon_r}}\tanh\left(j\frac{2\pi fd\sqrt{\mu_r\varepsilon_r}}{c}\right) \quad (6)$$

where Z_0 is the impedance of free space, Z_{in} is the normalized input characteristic impedance at the interface between atmosphere and absorber, μ_r is the relative complex permeability, ε_r is the relative complex permittivity, f is the frequency, d is the thickness of samples, c is the velocity of light (3×10^8 m/s). The effective absorption bandwidth (E_{AB}) is defined by the range of frequencies over which *RL* is smaller than −10 dB, which represents that 90% of the microwave energy is absorbed while only 10% of that is reflected [47].

3 Results and discussion

3. 1 Synthesis and microstructure of pure HE REB_6 powders

As shown in Fig. 1, rare earth hexaborides exhibit CsCl-type cubic structure with a space group of $Pm\bar{3}m$ (No. 221). The rare-earth and boron atoms are located at 1*a* (0, 0, 0) and 6*f* (0.5, 0.5, *z*) positions, respectively, where the position parameter *z* of B atom is related to the lattice parameter (*a*) and B–B bond lengths [48]. On the one hand, the structure of REB_6 is constructed by the strong covalent σ bonds that link boron octahedrons, which limits the change of the lattice parameters but only allows the adjustments of the lengths of inter-octahedra σ bond ($B–B_{inter}$) and intra-octahedron τ bond ($B–B_{intra}$) [19,23,24,33,49]. The changes in $B–B_{inter}$ and $B–B_{intra}$ distances have great impact on the electrical properties, leading to the electric conduction transition. Each boron octahedron in REB_6 is deficient of two electrons and thus the stability is ensured by the transformation of an electron from rare earth metals to boron octahedron, which give rise to good electrical conductivity in trivalent hexaborides [25,26,50]. As for the intriguing magnetism found in REB_6, the magnetic ordering might be attributed to an indirect exchange of the RKKY type via conduction electrons donated from trivalent rare-earth ions or impurities [51,52].

Figure 2 shows the XRD pattern of $(Ce_{0.2}Y_{0.2}Sm_{0.2}Er_{0.2}Yb_{0.2})B_6$ (HE REB_6-1) synthesized at 1900 ℃ for 1 h in vacuum. Standard ICDD/JCPDS cards of CeB_6, YB_6, SmB_6, ErB_6, and YbB_6 are also presented to confirm the formation of HE REB_6, which is structural ordered but compositional disordered with multi-principle RE elements.

To characterize the particle size and morphology, the HE REB_6-1 powders after grinding in an agate mortar are observed by SEM as shown in Fig. 3(a). The powders are equiaxial and the average particle size is about 1.86 μm as shown in Fig. 3(b).

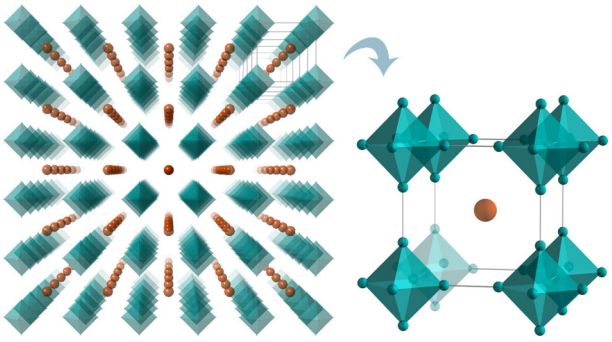

Fig. 1 Crystal structure of REB_6. Rare earth (RE) atoms (brown) and B_6 octahedron (cyan) are arranged in a CsCl-like packing.

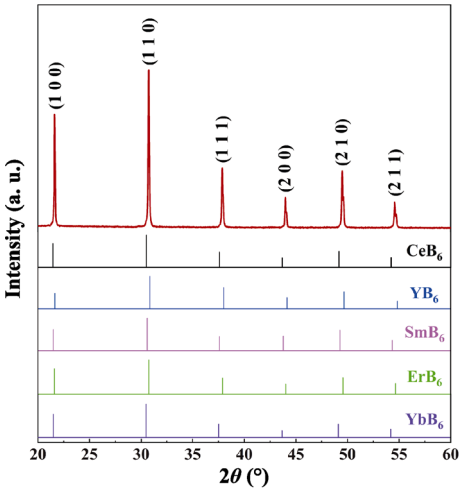

Fig. 2 XRD pattern of $(Ce_{0.2}Y_{0.2}Sm_{0.2}Er_{0.2}Yb_{0.2})B_6$ (HE REB_6-1) together with those of CeB_6, YB_6, SmB_6, ErB_6, and YbB_6 obtained from ICDD/JCPDS cards.

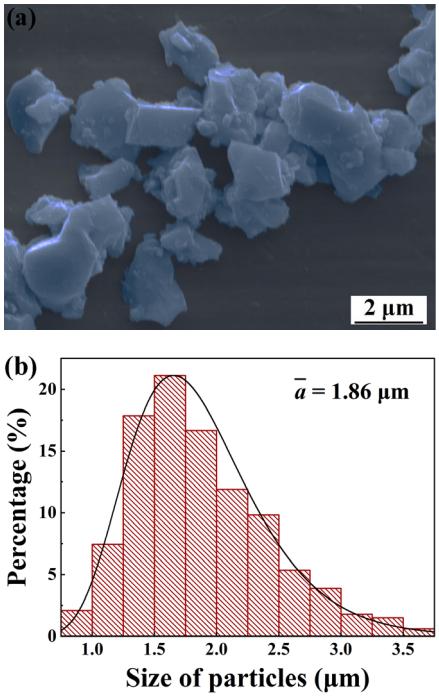

Fig. 3 (a) SEM image and (b) particle size distribution of $(Ce_{0.2}Y_{0.2}Sm_{0.2}Er_{0.2}Yb_{0.2})B_6$ powders.

Figure 4 compares the XRD patterns of five HE REB_6 synthesized at 1900 ℃ for 1 h in vacuum. The diffraction peaks of five samples show consistency in spite of different constituents, which indicate that single-phase high-entropy solid-solutions are formed among these rare-earth hexaborides. The lattice parameters of these HE REB_6 are calculated according to Bragg's law as shown in Eq. (7):

$$2d_{hkl} \cdot \sin\theta = \lambda \tag{7}$$

where λ = 1.5406 Å, θ is obtained from peak position of {100} by fitted Gaussian peak functions. The lattice parameter of a cubic lattice is equal to the interplanar spacing of {100} plane. Then the theoretical density is calculated by the lattice parameter. The lattice parameter (a) and theoretical density (ρ_{th}) of five HE REB_6 are listed in Table 3. The variation of lattice parameter is derived from the substitutions of RE elements, which leads to different degrees of lattice distortions. By replacing rare-earth ions (Y^{3+}, Sm^{3+}, Er^{3+} with ionic radius of 0.9 Å, 0.96 Å, 0.89 Å respectively) in HE REB_6-1 with Eu^{2+} (r = 1.17 Å), $(Ce_{0.2}Eu_{0.2}Sm_{0.2}Er_{0.2}Yb_{0.2})B_6$ (HE REB_6-2), $(Ce_{0.2}Y_{0.2}Eu_{0.2}Er_{0.2}Yb_{0.2})B_6$ (HE REB_6-3), and $(Ce_{0.2}Y_{0.2}Sm_{0.2}Eu_{0.2}Yb_{0.2})B_6$ (HE REB_6-4) with larger lattice parameters are obtained, which can be attributed to the substitution of Eu^{2+} that has larger ionic radius. Likewise, replacing Ce^{3+} (r = 0.87 Å) in HE REB_6-4 with Nd^{3+} (r = 0.98 Å) will lead to $(Nd_{0.2}Y_{0.2}Sm_{0.2}Eu_{0.2}Yb_{0.2})B_6$ (HE REB_6-5) with a larger lattice parameter.

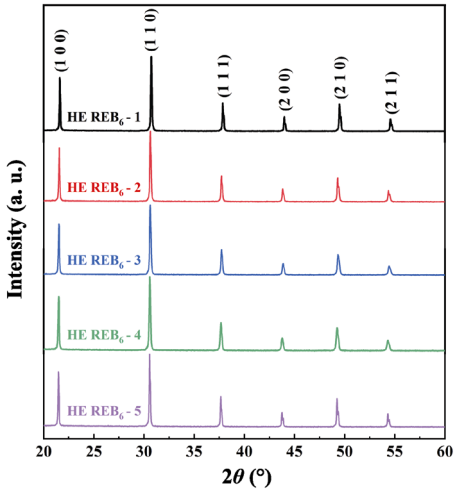

Fig. 4 XRD patterns of HE REB_6-1 $(Ce_{0.2}Y_{0.2}Sm_{0.2}Er_{0.2}Yb_{0.2})B_6$, HE REB_6-2 $(Ce_{0.2}Eu_{0.2}Sm_{0.2}Er_{0.2}Yb_{0.2})B_6$, HE REB_6-3 $(Ce_{0.2}Y_{0.2}Eu_{0.2}Er_{0.2}Yb_{0.2})B_6$, HE REB_6-4 $(Ce_{0.2}Y_{0.2}Sm_{0.2}Eu_{0.2}Yb_{0.2})B_6$, and HE REB_6-5 $(Nd_{0.2}Y_{0.2}Sm_{0.2}Eu_{0.2}Yb_{0.2})B_6$.

Table 3 Lattice parameter (a) and theoretical density (ρ_{th}) of HE REB_6

Hexaborides	Composition	a (Å)	ρ_{th} (g/cm^3)
HE REB_6-1	$(Ce_{0.2}Y_{0.2}Sm_{0.2}Er_{0.2}Yb_{0.2})B_6$	4.1092±0.0005	5.00
HE REB_6-2	$(Ce_{0.2}Eu_{0.2}Sm_{0.2}Er_{0.2}Yb_{0.2})B_6$	4.1215±0.0005	5.25
HE REB_6-3	$(Ce_{0.2}Y_{0.2}Eu_{0.2}Er_{0.2}Yb_{0.2})B_6$	4.1279±0.0005	4.94
HE REB_6-4	$(Ce_{0.2}Y_{0.2}Sm_{0.2}Eu_{0.2}Yb_{0.2})B_6$	4.1321±0.0005	4.84
HE REB_6-5	$(Nd_{0.2}Y_{0.2}Sm_{0.2}Eu_{0.2}Yb_{0.2})B_6$	4.1355±0.0005	4.85

3. 2 Synthesis and microstructure of HE REB_6/HE $REBO_3$ composite powders

From Fig. 5, standard ICDD/JCPDS cards of borates show that cerium borate exhibits orthorhombic aragonite-type structure which is different from the rest borates with hexagonal vaterite-type structure. After synthesized at 1600 ℃ for 1 h in Ar atmosphere, the main phases of the product are $(Ce_{0.2}Y_{0.2}Sm_{0.2}Er_{0.2}Yb_{0.2})B_6$ and $(Ce_{0.2}Y_{0.2}Sm_{0.2}Er_{0.2}Yb_{0.2})BO_3$, with the existence of a small amount of cerium borate and boron carbide, which is attributed to the uncompleted reduction.

Figure 6 presents the backscattered electron image (BSEI) and EDS patterns of two selected points in $(Ce_{0.2}Y_{0.2}Sm_{0.2}Er_{0.2}Yb_{0.2})B_6$/$(Ce_{0.2}Y_{0.2}Sm_{0.2}Er_{0.2}Yb_{0.2})BO_3$ composites. Through semi-quantitative analysis, the atomic ratio of O/B of two selected points in the golden phase and the blue phase are 1.602 and 0.018, respectively. Combining with XRD analysis, it can be concluded that the golden phase is HE $REBO_3$ and the blue phase is HE REB_6. Therefore, it comes to the conclusion that HE $REBO_3$ phase is distributed on the surface of HE REB_6 in HE REB_6/HE $REBO_3$ composite powders, as shown in Fig. 7.

Figure 8 shows the XRD patterns of the composite powders synthesized at 1600 ℃ for 1 h in Ar atmosphere. The diffraction peaks of these five composites are similar to each other and all can be indexed as vaterite-type structure although they possess different compositions. Therefore, it can be concluded

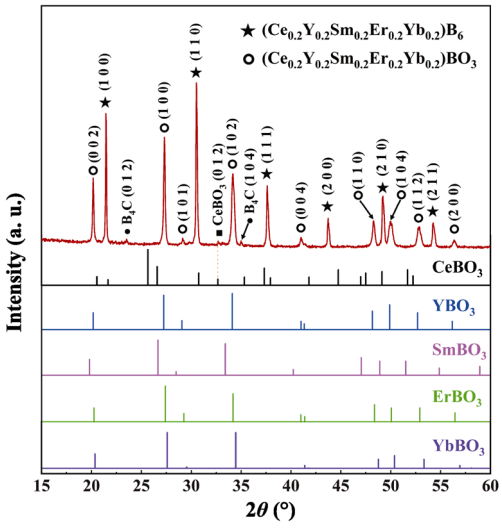

Fig. 5 XRD pattern of $(Ce_{0.2}Y_{0.2}Sm_{0.2}Er_{0.2}Yb_{0.2})B_6$ and $(Ce_{0.2}Y_{0.2}Sm_{0.2}Er_{0.2}Yb_{0.2})BO_3$ composite powders together with those of $CeBO_3$, YBO_3, $SmBO_3$, $ErBO_3$, and $YbBO_3$ obtained from ICDD/JCPDS cards.

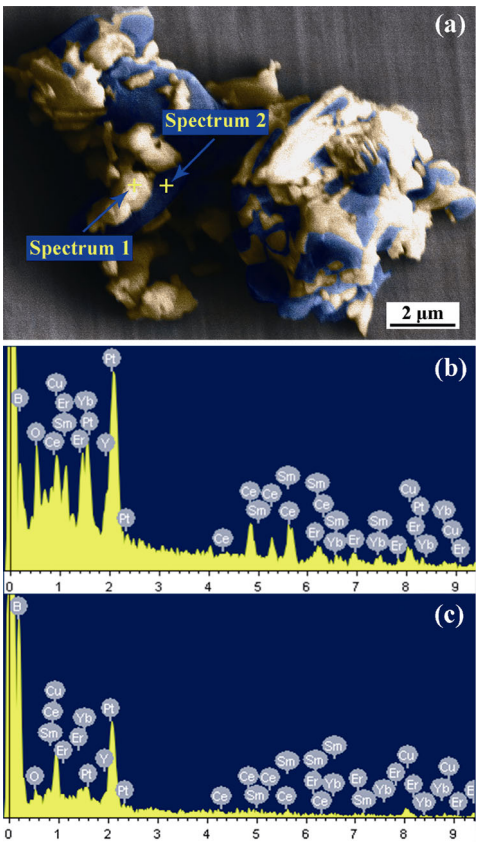

Fig. 6 (a) BESI of $(Ce_{0.2}Y_{0.2}Sm_{0.2}Er_{0.2}Yb_{0.2})B_6$/$(Ce_{0.2}Y_{0.2}Sm_{0.2}Er_{0.2}Yb_{0.2})BO_3$ composite powders, (b) EDS spectrum of selected point in the golden phase, and (c) EDS spectrum of the selected point in the blue phase.

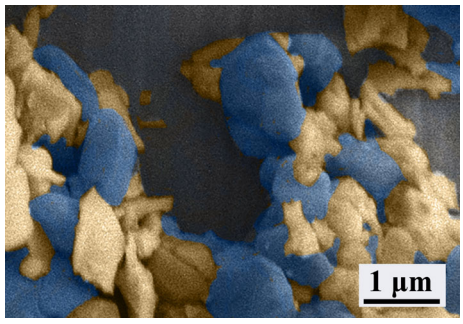

Fig. 7 BESI of $(Ce_{0.2}Y_{0.2}Sm_{0.2}Er_{0.2}Yb_{0.2})B_6$/$(Ce_{0.2}Y_{0.2}Sm_{0.2}Er_{0.2}Yb_{0.2})BO_3$ composite powers indicating the distribution of $(Ce_{0.2}Y_{0.2}Sm_{0.2}Er_{0.2}Yb_{0.2})BO_3$ phase (golden color).

that composites with HE REB_6 and HE $REBO_3$ phases are formed. Hereafter, the five composites synthesized at 1600 ℃ in Ar atmosphere are referred to as HE REB_6/HE $REBO_3$-1, HE REB_6/HE $REBO_3$-2, HE REB_6/HE $REBO_3$-3, HE REB_6/HE $REBO_3$-4, and HE REB_6/HE $REBO_3$-5, respectively. To estimate the relative content of different phases in these composites,

quantitative analysis was performed using the total pattern solution software (TOPAS). The weight fraction of HE $REBO_3$ and reliability factors, R_p and R_{wp}, are listed in Table 4.

3. 3 EM wave absorption properties

3.3.1 EM wave absorption properties of HE REB_6

Figure 9 reveals the frequency dependences of the electromagnetic parameters for HE REB_6/paraffin composites. As illustrated in Fig. 9(a) and Fig. 9(b), across the testing frequency range, the values of ε' and ε'' show a decreasing tendency from HE REB_6-1 to HE REB_6-4, which is attributed to the changes of electrical conductivity of HE REB_6 as a result of the changes of lattice constant a due to the substitution of Eu^{2+}. The decrease of lattice constant a will lead to the increasement of the bond length difference between $B–B_{inter}$ and $B–B_{intra}$, which will further give rise to the increasement of shear anisotropy. On this basis, REB_6 with smaller lattice constant would possess better electrical conductivity [49]. Therefore, the conductivity of HE REB_6 decreases from HE REB_6-1 to HE REB_6-4 as the lattice constant increases. In particularly, in exception of HE REB_6-3, ε'' values of HE REB_6 decrease with the increasing of frequency at low frequency, which indicates the dispersion phenomenon; while the value of ε'' exhibits growing tendency as the frequency increases. Generally,

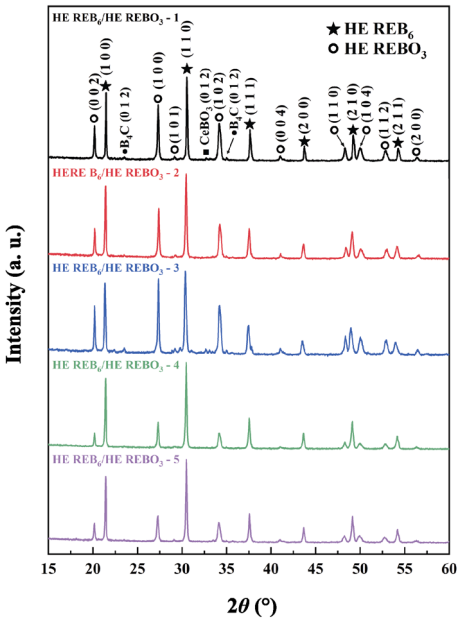

Fig. 8 XRD patterns of HE REB_6/HE $REBO_3$-1, HE REB_6/HE $REBO_3$-2, HE REB_6/HE $REBO_3$-3, HE REB_6/HE $REBO_3$-4, and HE REB_6/HE $REBO_3$-5 composite powders.

Table 4 Weight fraction of HE $REBO_3$ and reliability factors, R_p and R_{wp} in five HE REB_6/HE $REBO_3$ composites

Composites	Weight fraction of HE $REBO_3$ (%)	R_p (%)	R_{wp} (%)
HE REB_6/HE $REBO_3$-1	58.34	8.49	14.69
HE REB_6/HE $REBO_3$-2	49.22	7.25	11.93
HE REB_6/HE $REBO_3$-3	64.78	8.32	14.69
HE REB_6/HE $REBO_3$-4	38.67	7.95	13.26
HE REB_6/HE $REBO_3$-5	41.95	6.90	10.85

the magnitude of dielectric loss can be estimated by the dielectric loss tangent ($\tan\delta_\varepsilon = \frac{\varepsilon''}{\varepsilon'}$). From Fig. 10(a), the variation of dielectric loss tangent shows a similar tendency to that of ε'' value. It is expected that HE REB_6-1 and HE REB_6-2 have considerable dielectric loss ability, which is derived from dipolar polarization, conduction loss, and polarization loss [53,54]. In specific, numerous dipoles in HE REB_6 can provide multiple ways for the transmission of the electromagnetic wave [55]. Moreover, abundant polarization charges and a sufficient number of interfaces between the HE REB_6 ceramics and paraffin wax are beneficial to spur interfacial polarization (called the Maxwell–Wagner effect) and related relaxation, which contribute to the dielectric loss [56,57]. The electron migration because of natural electrical conductivity will also lead to the reduction of electromagnetic energy. The polarization mechanism can be described in the assist of Debye theory [58] as shown in Eq. (8):

$$\left(\varepsilon' - \frac{\varepsilon_s + \varepsilon_\infty}{2}\right)^2 + (\varepsilon'')^2 = \left(\frac{\varepsilon_s - \varepsilon_\infty}{2}\right)^2 \quad (8)$$

where ε_s, ε_∞ are the static permittivity, and relative dielectric permittivity at high-frequency limit, respectively. Therefore, the relationship between ε' and ε'' is represented by a curve in the shape of semicircle (called the Cole–Cole semicircle), and each semicircle corresponds to one Debye relaxation process [59]. Figure 10(b) presents the ε'–ε'' plots of HE REB_6, where clear semicircles are pictured to reflect the polarization relaxations of HE REB_6 powders.

The relative complex permeability and magnetic loss tangent of HE REB_6 are shown in Figs. 9(c), 9(d), and 10(c). From Fig. 9(c), the μ' values of HE REB_6-2, HE REB_6-4, and HE REB_6-5 decrease in the range of 2–8 GHz and then remain steady because of the relaxation of magnetic moments procession, while those

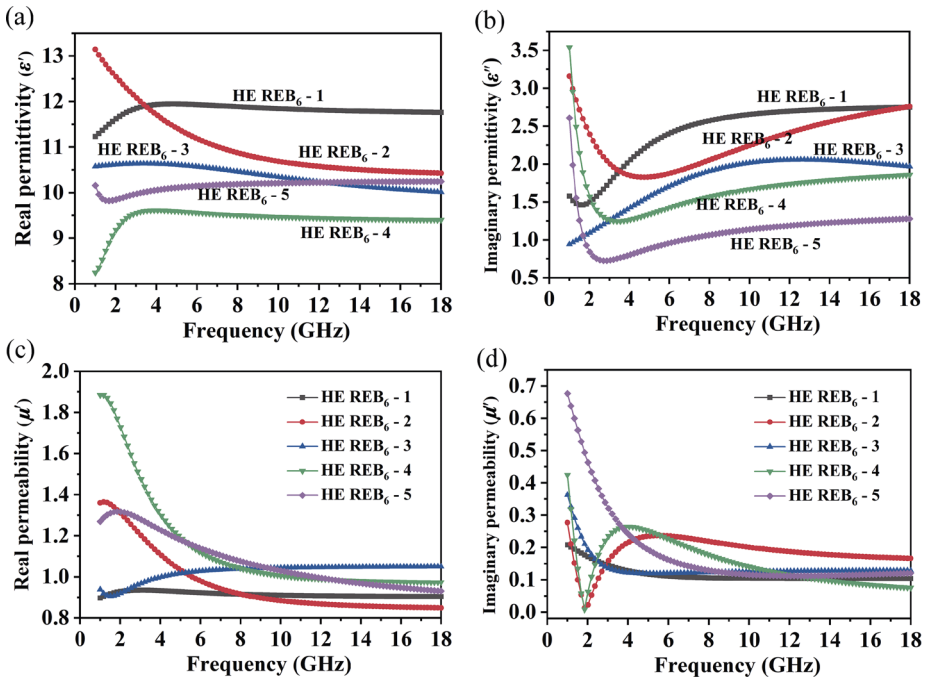

Fig. 9 Electromagnetic parameters of HE REB_6: (a) real permittivity (ε'), (b) imaginary permittivity (ε''), (c) real permeability (μ'), (d) imaginary permeability (μ'').

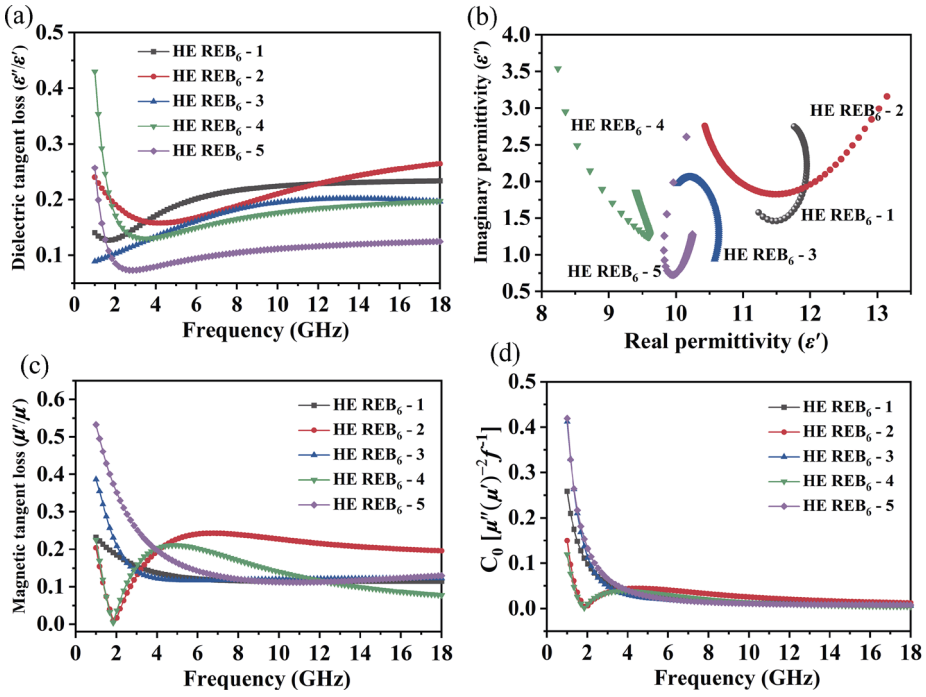

Fig. 10 Frequency dependences of (a) the dielectric loss tangent ($\varepsilon''/\varepsilon'$) and (c) the magnetic loss tangent (μ''/μ'); (b) Cole–Cole semicircles and (d) C_0–f curves of HE REB_6.

of HE REB_6-1 and HE REB_6-3 exhibit a small amount of increasement. Figure 9(d) shows frequency dependent of μ'' of HE REB_6. Resonance peaks are observed, which can be described by natural resonance [60]. The corresponding values of magnetic loss tangent of HE REB_6 exhibit similar fluctuation with μ'' values. Generally, the magnetic loss is derived from hysteresis loss, domain wall displacement loss, natural resonance loss, and eddy current loss [61]. Since the characterization is performed in a weak external

magnetic field at the frequency range of gigahertz, hysteresis loss and domain wall displacement loss can be ruled out from the mechanism of magnetic loss in HE REB_6. The contribution of Eddy current loss to the reflected loss is related to the electrical conductivity of materials (σ) and the matching thickness (d), as represented by Eq. (9) [62]:

$$\mu'' \approx \frac{2}{3}\pi\mu_0(\mu')d^2 f\sigma \tag{9}$$

where μ_0 is the vacuum permeability. If the eddy current loss is the dominate factor for the magnetic loss, the value of C_0 ($C_0 = \mu''(\mu')^{-2} f^{-1}$) should be a constant [63]; otherwise, the natural resonance loss is preponderance. Figure 10(d) presents the values of C_0 of HE REB_6 as a function of frequency. In the frequency range of 1–12 GHz, the values of C_0 decrease with the increase of frequency. With raising frequency, the values of C_0 remain as a constant. Therefore, it can be concluded that both the eddy current loss and the natural resonance loss contribute to the magnetic loss. It is worth noting that the μ'' values of HE REB_6 in Fig. 9(d) are close to that of Fe_3O_4, which is a typical magnetic EM wave absorber with exceptional magnetic features [64,65]. Drawn from the analysis of dielectric and magnetic loss tangents, it is concluded that the absorption abilities of HE REB_6 are generated by the coupling of dielectric and magnetic losses.

Based on above discussions, high electric and magnetic loss tangents will lead to high reflection loss (RL), which is one of the vital evaluation indexes of the EM wave absorption abilities. With relatively higher dielectric and magnetic loss tangents, HE REB_6-2 might possess the highest RL value. However, from Fig. 11(a), it can be found that HE REB_6-1 rather than HE REB_6-2 exhibits the highest RL value, which is due to the better impedance match. It has come to light that the closer the impedance match values to 1, the better the impedance match [66]. From this angle, HE REB_6-1 possesses the best impedance matching, and HE REB_6-2 ranks the second, as shown in Fig. 11(b). As shown in Figs. 11(a) and 11(c), the RL_{min} value of HE REB_6-1 reaches –33.4 dB at 11.5 GHz with a thickness of 2 mm, and the optimized effective absorption bandwidth (E_{AB}) is 3.9 GHz from 13.6 to 17.5 GHz with a thickness of 1.5 mm. As shown in Fig. 11(d), HE REB_6-2 reaches the largest E_{AB} of 4.3 GHz from 12.6 to 16.9 GHz at thickness of 1.7 mm. Therefore, the superior EM absorption properties require not only strong absorption, but also good impedance matching. In addition, the variation of impedance match values of HE REB_6 indicates the impedance matching can be tuned via compositional design. The addition of multi-principle elements with different atomic sizes in rare-earth hexaborides brings about severe lattice

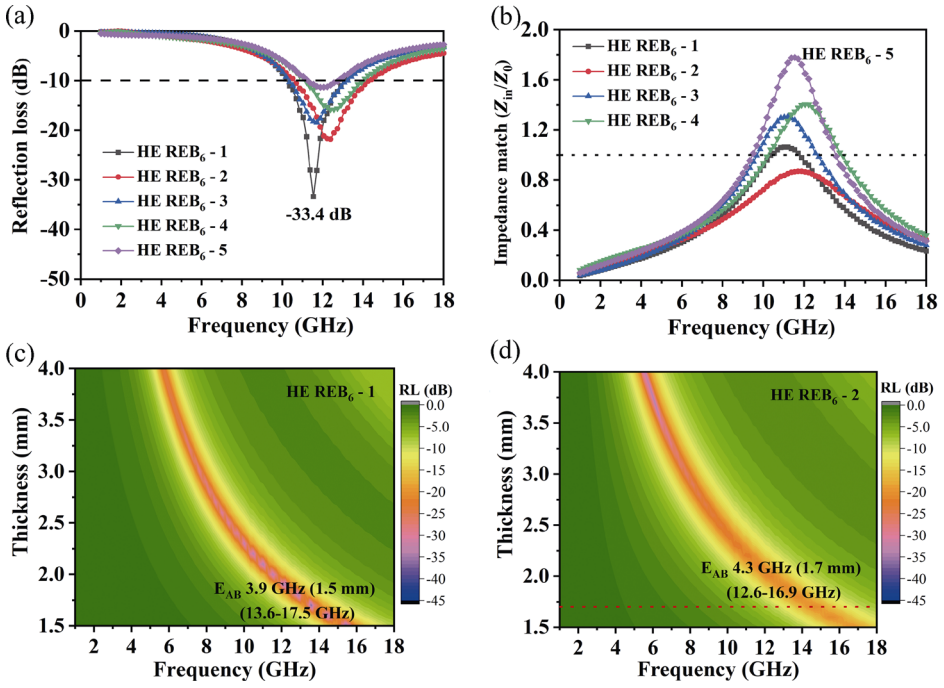

Fig. 11 Comparison of (a) reflection loss (RL) values and (b) impedance match (Z_{in}/Z_0) for HE REB_6. (c) and (d) Frequency dependence of RL values at various thickness for HE REB_6-1 and HE REB_6-2, respectively.

distortion effect, which has an impact on the changes of B–B bonding lengths and electronic structure [25,26]. Thus, different electronic conductivity and magnetic performance in HE REB_6 can be achieved through composition design, which will lead to the difference of EM wave absorption properties in HE REB_6 with different constituent.

3.3.2 EM wave absorption properties of HE REB_6/HE $REBO_3$

Combining the microstructure shown in Fig. 7 and the XRD patterns of HE REB_6/HE $REBO_3$ powders shown in Fig. 8, it comes to the conclusion that composites of HE REB_6 and HE $REBO_3$ are formed. From Fig. 12(a), except for HE REB_6/HE $REBO_3$-4, ε' values of HE composites are smaller than those of HE REB_6 in the whole frequency range, indicating that the conductivity is reduced because of the instinct insulating feature of HE $REBO_3$, which will further decrease ε'' value according to free electron theory $\varepsilon'' \approx \sigma/(2\pi f \varepsilon_0)$, where σ is the conductivity and ε_0 is the permittivity of vacuum [67]. However, as shown in Fig. 12(b), the considerable improvement of ε'' value of HE REB_6/HE $REBO_3$ compared with those of HE REB_6 are observed, which indicates that there is another dominant mechanism contributing to electric loss. In specific, the coverage of HE $REBO_3$ intermediate phase will spur more interfacial polarizations and related relaxations among HE REB_6, HE $REBO_3$ and paraffin wax phases, which will lead to more severe interface polarization under the action of electromagnetic waves. Therefore, compared to HE REB_6 samples, the values of electric dissipation factor ($\varepsilon''/\varepsilon'$) of HE REB_6/HE $REBO_3$ samples are higher (Fig. 13(a)). As for the permeability shown in Figs. 12(c) and 12(d), the μ' values of HE REB_6/HE $REBO_3$ are close to those of HE REB_6, while the μ'' values are lower than those of HE REB_6. According to Eq. (9), the decrease of electrical conductivity due to the formation of instinct insulating HE $REBO_3$ phase will give rise to reduction of μ'' value. Then, from Fig. 13(c), the magnetic loss tangent (μ''/μ') of HE REB_6/HE $REBO_3$ samples is reduced, which indicates relatively lower magnetic loss. These foregoing results indicate that both dielectric loss and magnetic loss of HE REB_6/HE $REBO_3$ contribute to dissipating the electromagnetic wave energy, but the dominant effect is due to the dielectric loss.

The dielectric loss is caused by Debye dipolar relaxation [59], which is proven by the presence of semicircle curves as shown in Fig. 13(b). The C_0 values in Fig. 13(d) decrease dramatically as frequency increase in the frequency range of 1–6 GHz; then, they keep unchanged as the frequency increases. Therefore, the magnetic loss is derived from eddy current loss and

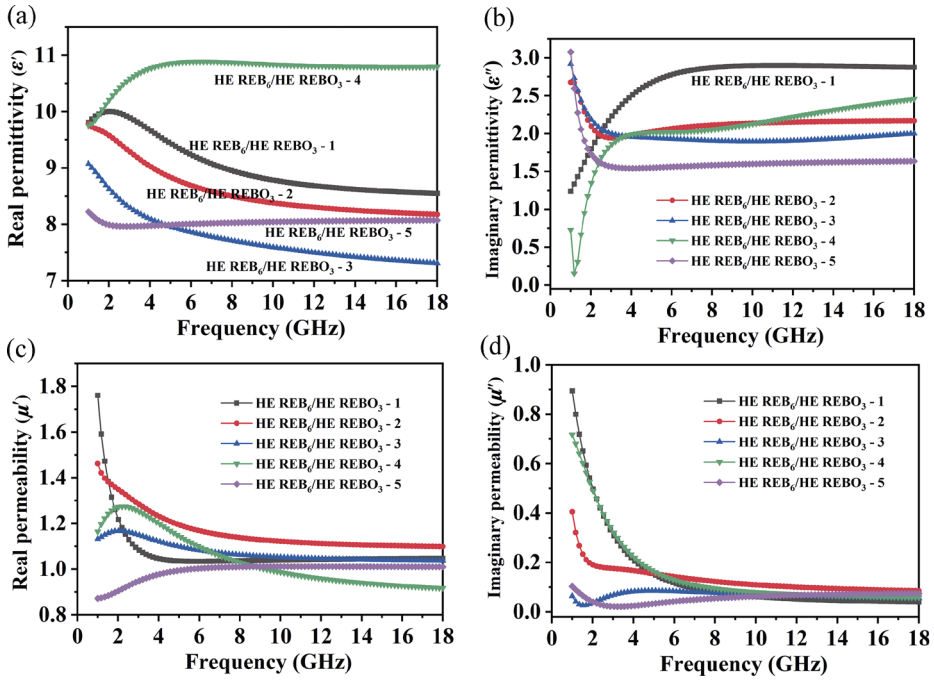

Fig. 12 Electromagnetic parameters of HE REB_6/HE $REBO_3$: (a) real permittivity (ε'), (b) imaginary permittivity (ε''), (c) real permeability (μ'), (d) imaginary permeability (μ'').

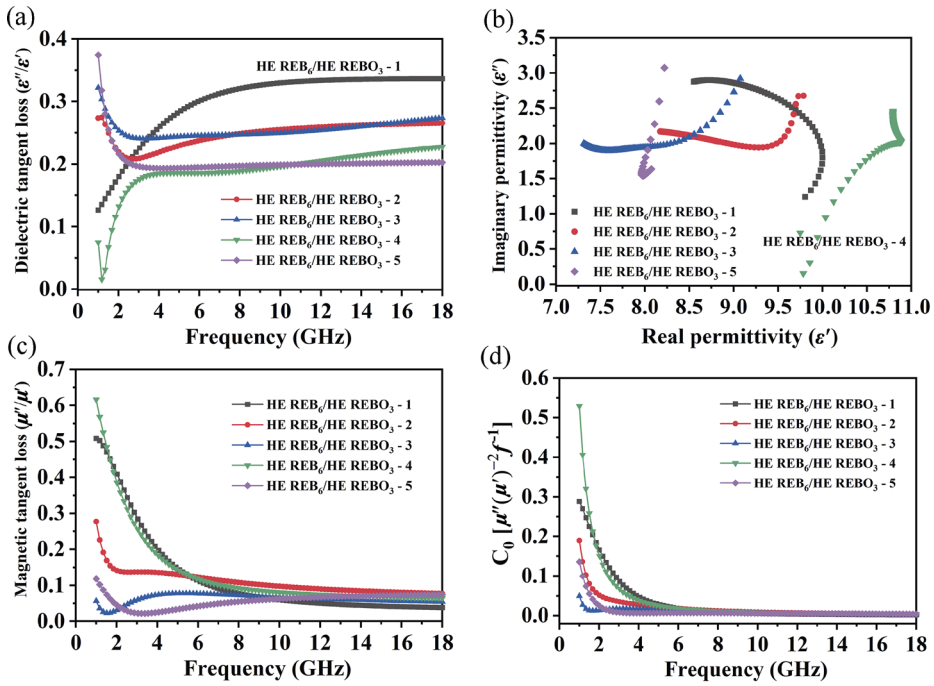

Fig. 13 Frequency dependences of (a) the dielectric loss tangent ($\varepsilon''/\varepsilon'$) and (c) the magnetic loss tangent (μ''/μ'); (b) Cole–Cole semicircles and (d) C_0–f curves of HE REB_6/HE $REBO_3$.

natural resonance loss [60,63]. As has been discussed in the previous section, the EM wave absorption properties are strongly affected by the impedance match. Otherwise, electromagnetic wave will be reflected on the surface of the EM wave absorbing materials, and the reflect loss ability is in vain when it comes to the fact that the entering of EM wave into the absorber is difficult to realize [68]. Therefore, the reduction of reflection losses of HE REB_6/HE $REBO_3$ composite powders shown in Fig. 14(a) is due to the unfitting impedance match compared with those of HE REB_6 samples. For example, from Fig. 14(a), the value of impedance match (Z_{in}/Z_0) of HE REB_6-1 and HE REB_6/HE $REBO_3$-1 increases from 1.06 to 1.19, which gives rise to reduction of the RL_{min} value from –33.4 to –24.1 dB with the same thickness of 2 mm.

Although the reflection loss abilities of HE REB_6/HE $REBO_3$ samples become weaker, HE REB_6/HE $REBO_3$ composite powders still exhibit considerable effective absorption bandwidth with low thickness. As shown in Figs. 14(c) and 14(d), both HE REB_6/HE $REBO_3$-1 and HE REB_6/HE $REBO_3$-2 exhibit wide E_{AB} of 4.1 GHz with the same width of 1.7 mm. Thus, the introduction of HE $REBO_3$ as an intermediate phase into HE REB_6 will lead to greater dielectric loss, relatively poorer magnetic loss, and worsen impedance matching. For example, in the frequency range of 10–14 GHz, the value of dielectric tangent loss of HE REB_6/HE $REBO_3$-1 reaches 0.35 which is 1.75 times of that of HE REB_6-1, while the value of magnetic tangent loss decreases from 0.12 to 0.05, and the value of impedance match (Z_{in}/Z_0) gets further away from 1. As a result, the value of RL_{min} of HE REB_6/HE $REBO_3$-1 decreases, which indicates that the EM wave absorption abilities become weaker. The above results infer that although the coverage of insulator HE $REBO_3$ phase is beneficial to spur interfacial polarization and related relaxation and give rise to greater dielectric loss, worsen of the magnetic loss and impedance matching, which will finally lead to the weaken of overall reflection loss ability.

Figure 15 summarizes the optimized E_{AB} value and the sample thickness of some reported EM absorbing materials of various kinds (SiC based [69–73], carbons based [74–78], ferrite metal-organic framework (Fe-MOF) [47], phosphides based [79], sulfides based [68,80], polymers based [81–83], metals/alloys based [62,63,67, 84,85], and oxides based materials [64,66,86–89]). As we have mentioned in previous sections, seeking for materials with thin thickness and wide effective bandwidth is the trend for the development of EM wave absorbing materials. From this aspect, searching for materials in region II are the purposes of many researches. As shown in Fig. 15, although materials in

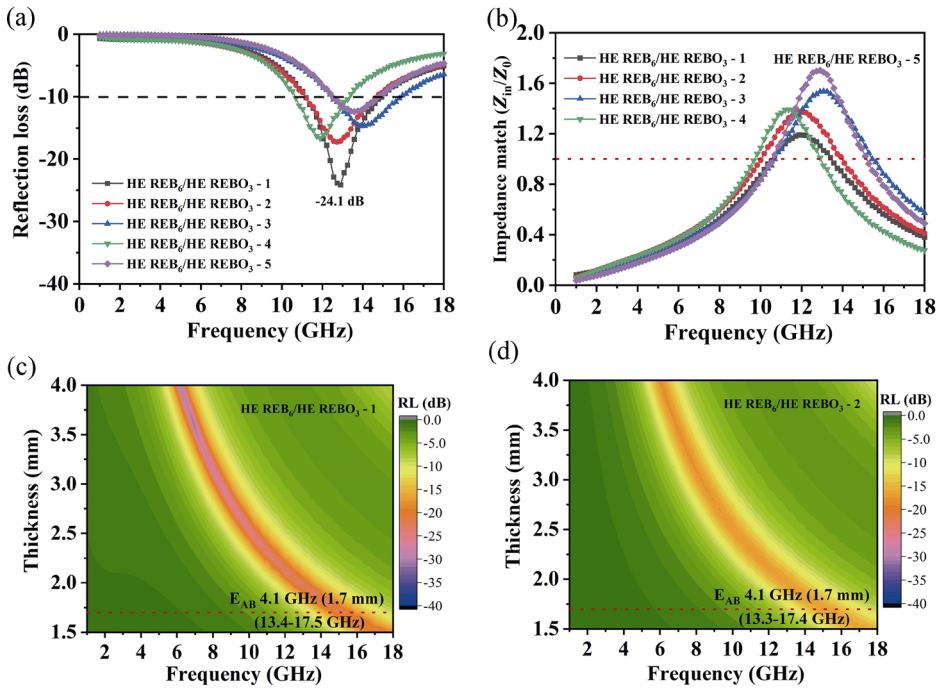

Fig. 14 Comparison of (a) reflection loss (*RL*) values and (b) impedance match (Z_{in}/Z_0) for HE REB_6/HE $REBO_3$. (c, d) Frequency dependence of *RL* values at various thickness for HE REB_6/HE $REBO_3$-1 and HE REB_6/HE $REBO_3$-2, respectively.

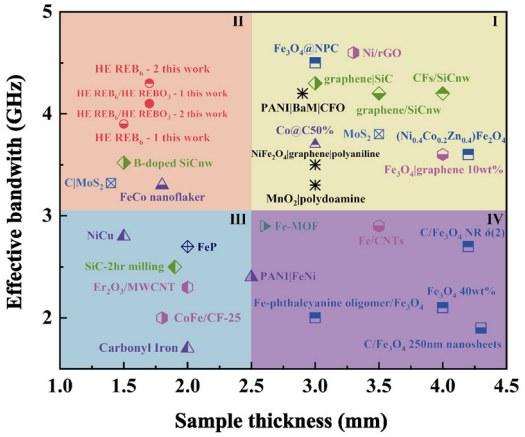

Fig. 15 Effective bandwidth and corresponding sample thickness of various kinds of reported EM absorbing materials.

region I possess wide E_{AB}, they are still restricted by thicker thickness. In contract, while materials in region III exhibit small thickness, their narrow effective bandwidth is the hindrances. As is self-evident, materials in region IV have disadvantages of both heavy thickness and narrow E_{AB}. It is worthy of noting that HE REB_6-1, HE REB_6-2, HE REB_6/HE $REBO_3$-1, and HE REB_6/HE $REBO_3$-2 are located in region II, which exhibit wide E_{AB} with considerable thin thickness, indicating their superior EM wave absorption properties among these materials.

4 Conclusions

In conclusion, five HE REB_6 powders including $(Ce_{0.2}Y_{0.2}Sm_{0.2}Er_{0.2}Yb_{0.2})B_6$, $(Ce_{0.2}Eu_{0.2}Sm_{0.2}Er_{0.2}Yb_{0.2})B_6$, $(Ce_{0.2}Y_{0.2}Eu_{0.2}Er_{0.2}Yb_{0.2})B_6$, $(Ce_{0.2}Y_{0.2}Sm_{0.2}Eu_{0.2}Yb_{0.2})B_6$, and $(Nd_{0.2}Y_{0.2}Sm_{0.2}Eu_{0.2}Yb_{0.2})B_6$ as well as five HE REB_6/HE $REBO_3$ composite powders including $(Ce_{0.2}Y_{0.2}Sm_{0.2}Er_{0.2}Yb_{0.2})B_6/(Ce_{0.2}Y_{0.2}Sm_{0.2}Er_{0.2}Yb_{0.2})BO_3$, $(Ce_{0.2}Eu_{0.2}Sm_{0.2}Er_{0.2}Yb_{0.2})B_6/(Ce_{0.2}Eu_{0.2}Sm_{0.2}Er_{0.2}Yb_{0.2})BO_3$, $(Ce_{0.2}Y_{0.2}\ Eu_{0.2}Er_{0.2}Yb_{0.2})B_6/(Ce_{0.2}Y_{0.2}Eu_{0.2}Er_{0.2}Yb_{0.2})BO_3$, $(Ce_{0.2}Y_{0.2}Sm_{0.2}Eu_{0.2}Yb_{0.2})B_6/(Ce_{0.2}Y_{0.2}Sm_{0.2}Eu_{0.2}Yb_{0.2})BO_3$, and $(Nd_{0.2}Y_{0.2}Sm_{0.2}Eu_{0.2}Yb_{0.2})B_6/(Nd_{0.2}Y_{0.2}Sm_{0.2}Eu_{0.2}Yb_{0.2})BO_3$ were designed and successfully synthesized through a facile one-step boron carbide reduction method. XRD analysis reveals that the five as-synthesized HE REB_6 are phase-pure solid solutions with CsCl-type cubic structure, and the five as-synthesized HE REB_6/HE $REBO_3$ contain two main phases of HE REB_6 and HE $REBO_3$. The theoretical density of HE REB_6 ranges from 4.84 to 5.25 g/cm^3. The weight fraction of HE $REBO_3$ in HE REB_6/HE $REBO_3$ composite powders was estimated through quantitative phase analysis to be ranging from 38.67% to 64.78%. SEM analysis indicates that the $(Ce_{0.2}Y_{0.2}Sm_{0.2}Er_{0.2}Yb_{0.2})B_6$ powders possess equiaxial morphology with the mean particle size of 1.86 μm and HE $REBO_3$ is distributed on the surface of HE REB_6 phases in HE REB_6/HE $REBO_3$ composite

powders.

The synergetic effects of dielectric and magnetic losses and tunable impedance matching are attributed to favorable EM wave absorption properties. The RL_{min} value of HE REB_6-1 reaches –33.4 dB at 11.5 GHz at thickness of 2 mm, and the optimized effective absorption bandwidth (E_{AB}) is 3.9 GHz from 13.6–17.5 GHz at thickness of 1.5 mm. The introduction of HE $REBO_3$ as an intermediate phase into HE REB_6 leads to greater dielectric loss, relatively poor magnetic loss, and worse impedance matching, which further leads to the reduction of EM wave reflection loss ability in HE REB_6/HE $REBO_3$ composite powders. Although the RL_{min} value of HE REB_6/HE $REBO_3$-1 decreases to –24.1 dB, it still reaches wide E_{AB} of 4.1 GHz from 13.4–17.5 GHz at thin thickness of 1.7 mm. Single-phase HE REB_6 ceramics with coupling of dielectric and magnetic losses possess thin thickness, wide effective absorption bandwidth, and considerable EM absorption capability. Combining good high-temperature stability, oxidation and corrosion resistance, lightweight HE REB_6 ceramics are promising as a new type of EM absorbing materials that can meet the requirements of high temperature or corrosive serving environments.

Acknowledgements

We gratefully acknowledge financial supports from the National Natural Science Foundation of China under Grant Nos. 51972089, 51672064, and U1435206.

References

[1] Chung DDL. Electromagnetic interference shielding effectiveness of carbon materials. *Carbon* 2001, **39**: 279–285.

[2] Holloway CL, DeLyser RR, German RF, *et al*. Comparison of electromagnetic absorber used in anechoic and semi-anechoic chambers for emissions and immunity testing of digital devices. *IEEE Trans Electromagn Compat* 1997, **39**: 33–47.

[3] Wang C, Murugadoss V, Kong J, *et al*. Overview of carbon nanostructures and nanocomposites for electromagnetic wave shielding. *Carbon* 2018, **140**: 696–733.

[4] Jia YJ, Chowdhury MAR, Zhang DJ, *et al*. Wide-band tunable microwave-absorbing ceramic composites made of polymer-derived SiOC ceramic and *in situ* partially surface-oxidized ultra-high-temperature ceramics. *ACS Appl Mater Interfaces* 2019, **11**: 45862–45874.

[5] Jia ZR, Lin KJ, Wu GL, *et al*. Recent progresses of high-temperature microwave-absorbing materials. *Nano* 2018, **13**: 1830005.

[6] Wallace JL. Broadband magnetic microwave absorbers: Fundamental limitations. *IEEE Trans Magn* 1993, **29**: 4209–4214.

[7] Adebayo LL, Soleimani H, Yahya N, *et al*. Recent advances in the development of Fe_3O_4-based microwave absorbing materials. *Ceram Int* 2020, **46**: 1249–1268.

[8] Wu NN, Liu C, Xu DM, *et al*. Enhanced electromagnetic wave absorption of three-dimensional porous Fe_3O_4/C composite flowers. *ACS Sustainable Chem Eng* 2018, **6**: 12471–12480.

[9] Li YJ, Yu M, Yang PG, *et al*. Enhanced microwave absorption property of Fe nanoparticles encapsulated within reduced graphene oxide with different thicknesses. *Ind Eng Chem Res* 2017, **56**: 8872–8879.

[10] Liu Q, Liu H, Han M, *et al*. Nanometer-sized nickel hollow spheres. *Adv Mater* 2005, **17**: 1995–1999.

[11] Zhang Y, Huang Y, Zhang TF, *et al*. Broadband and tunable high-performance microwave absorption of an ultralight and highly compressible graphene foam. *Adv Mater* 2015, **27**: 2049–2053.

[12] Yan LL, Wang XX, Zhao SC, *et al*. Highly efficient microwave absorption of magnetic nanospindle–conductive polymer hybrids by molecular layer deposition. *ACS Appl Mater Interfaces* 2017, **9**: 11116–11125.

[13] Zhang P, Han XJ, Kang LL, *et al*. Synthesis and characterization of polyaniline nanoparticles with enhanced microwave absorption. *RSC Adv* 2013, **3**: 12694–12701.

[14] Kumar S, Chatterjee R. Complex permittivity, permeability, magnetic and microwave absorbing properties of Bi^{3+} substituted U-type hexaferrite. *J Magn Magn Mater* 2018, **448**: 88–93.

[15] Park K, Lee S, Kim C, *et al*. Fabrication and electromagnetic characteristics of electromagnetic wave absorbing sandwich structures. *Compos Sci Technol* 2006, **66**: 576–584.

[16] Zong M, Huang Y, Ding X, *et al*. One-step hydrothermal synthesis and microwave electromagnetic properties of RGO/$NiFe_2O_4$ composite. *Ceram Int* 2014, **40**: 6821–6828.

[17] Petrov VM, Gagulin VV. Microwave absorbing materials. *Inorg Mater* 2001, **37**: 93–98.

[18] Etourneau J, Hagenmuller P. Structure and physical features of the rare-earth borides. *Philos Mag B* 1985, **52**: 589–610.

[19] Longuet-Higgins HC, Roberts MDV. The electronic structure of the borides MB_6. *Proc R Soc Lond A* 1954, **224**: 336–347.

[20] Yamazaki M. Group-theoretical treatment of the energy bands in metal borides MeB_6. *J Phys Soc Jpn* 1957, **12**: 1–6.

[21] Aronson MC, Sarrao JL, Fisk Z, *et al*. Fermi surface of the ferromagnetic semimetal, EuB_6. *Phys Rev B* 1999, **59**: 4720–4724.

[22] Walch PF, Ellis DE, Mueller FM. Energy bands and bonding in LaB_6 and YB_6. *Phys Rev B* 1977, **15**: 1859–1866.

[23] Kher SS, Spencer JT. Chemical vapor deposition of metal borides. *J Phys Chem Solids* 1998, **59**: 1343–1351.
[24] Spear KE. Phase behavior and related properties of rare-earth borides. In *Phase Diagrams: Materials Science and Technology.* Alper AM, Ed. New York: Academic Press, 1976: 91–159.
[25] Mercurio JP, Etourneau J, Naslain R, *et al*. Electrical and magnetic properties of some rare-earth hexaborides. *J Less-Common Met* 1976, **47**: 175–180.
[26] MacKinnon IDR, Alarco JA, Talbot PC. Metal hexaborides with Sc, Ti or Mn. *Model Numer Simul Mater Sci* 2013, **3**: 158–169.
[27] Bachmann R, Lee KN, Geballe TH, *et al*. Spin scattering and magnetic ordering in EuB_6. *J Appl Phys* 1970, **41**: 1431–1432.
[28] Geballe TH, Matthias BT, Andres K, *et al*. Magnetic ordering in the rare-earth hexaborides. *Science* 1968, **160**: 1443–1444.
[29] Hacker Jr. H, Shimada Y, Chung KS. Magnetic properties of CeB_6, PrB_6, EuB_6, and GdB_6. *Phys Stat Sol (a)* 1971, **4**: 459–465.
[30] Matsubayashi K, Maki M, Tsuzuki T, *et al*. Parasitic ferromagnetism in a hexaboride? *Nature* 2002, **420**: 143–144.
[31] Matthias BT, Geballe TH, Andres K, *et al*. Superconductivity and antiferromagnetism in boron-rich lattices. *Science* 1968, **159**: 530.
[32] Young DP, Hall D, Torelli ME, *et al*. High-temperature weak ferromagnetism in a low-density free-electron gas. *Nature* 1999, **397**: 412–414.
[33] Olsen GH, Cafiero AV. Single-crystal growth of mixed (La, Eu, Y, Ce, Ba, Cs) hexaborides for thermionic emission. *J Cryst Growth* 1978, **44**: 287–290.
[34] Liu Y, Lu WJ, Qin JN, *et al*. A new route for the synthesis of NdB_6 powder from Nd_2O_3–B_4C system. *J Alloys Compd* 2007, **431**: 337–341.
[35] Hasan M, Sugo H, Kisi E. Low temperature carbothermal and boron carbide reduction synthesis of LaB_6. *J Alloys Compd* 2013, **578**: 176–182.
[36] Rost CM, Sachet E, Borman T, *et al*. Entropy-stabilized oxides. *Nat Commun* 2015, **6**: 8485.
[37] Braun JL, Rost CM, Lim M, *et al*. Charge-induced disorder controls the thermal conductivity of entropy-stabilized oxides. *Adv Mater* 2018, **30**: 1805004.
[38] Zhao ZF, Xiang HM, Dai FZ, *et al*. $(TiZrHf)P_2O_7$: An equimolar multicomponent or high entropy ceramic with good thermal stability and low thermal conductivity. *J Mater Sci Technol* 2019, **35**: 2227–2231.
[39] Chen H, Xiang HM, Dai FZ, *et al*. High porosity and low thermal conductivity high entropy $(Zr_{0.2}Hf_{0.2}Ti_{0.2}Nb_{0.2}Ta_{0.2})C$. *J Mater Sci Technol* 2019, **35**: 1700–1705.
[40] Chen H, Xiang HM, Dai FZ, *et al*. High entropy $(Yb_{0.25}Y_{0.25}Lu_{0.25}Er_{0.25})_2SiO_5$ with strong anisotropy in thermal expansion. *J Mater Sci Technol* 2020, **36**: 134–139.
[41] Zhao ZF, Chen H, Xiang HM, *et al*. $(Y_{0.25}Yb_{0.25}Er_{0.25}Lu_{0.25})_2(Zr_{0.5}Hf_{0.5})_2O_7$: A defective fluorite structured high entropy ceramic with low thermal conductivity and close thermal expansion coefficient to Al_2O_3. *J Mater Sci Technol* 2020, **39**: 167–172.
[42] Zhao ZF, Chen H, Xiang HM, *et al*. High entropy defective fluorite structured rare-earth niobates and tantalates for thermal barrier applications. *J Adv Ceram* 2020, **9**: 303–311.
[43] Chen H, Zhao B, Zhao ZF, *et al*. Achieving strong microwave absorption capability and wide absorption bandwidth through a combination of high entropy rare earth silicide carbides/rare earth oxides. *J Mater Sci Technol* 2020, **47**: 216–222.
[44] Shannon RD. Revised effective ionic radii and systematic studies of interatomic distances in halides and chalcogenides. *Acta Cryst A* 1976, **32**: 751–767.
[45] Sarkar A, Loho C, Velasco L, *et al*. Multicomponent equiatomic rare earth oxides with a narrow band gap and associated praseodymium multivalency. *Dalton Trans* 2017, **46**: 12167–12176.
[46] Miles PA, Westphal WB, von Hippel A. Dielectric spectroscopy of ferromagnetic semiconductors. *Rev Mod Phys* 1957, **29**: 279–307.
[47] Green M, Liu Z, Xiang P, *et al*. Ferric metal-organic framework for microwave absorption. *Mater Today Chem* 2018, **9**: 140–148.
[48] Zhou YC, Dai FZ, Xiang HM, *et al*. Shear anisotropy: Tuning high temperature metal hexaborides from soft to extremely hard. *J Mater Sci Technol* 2017, **33**: 1371–1377.
[49] Zhou YC, Liu B, Xiang HM, *et al*. YB_6: A 'ductile' and soft ceramic with strong heterogeneous chemical bonding for ultrahigh-temperature applications. *Mater Res Lett* 2015, **3**: 210–215.
[50] Grechnev GE, Baranovskiy AE, Fil VD, *et al*. Electronic structure and bulk properties of MB_6 and MB_{12} borides. *Low Temp Phys* 2008, **34**: 921–929.
[51] Mercurio JP, Etourneau J, Naslain R, *et al*. Electrical and magnetic properties of some rare-earth hexaborides. *J Less-Common Met* 1976, **47**: 175–180.
[52] Kuneš J, Pickett WE. Kondo and anti-Kondo coupling to local moments in EuB_6. *Phys Rev B* 2004, **69**: 165111.
[53] Tian LH, Yan XD, Xu JL, *et al*. Effect of hydrogenation on the microwave absorption properties of $BaTiO_3$ nanoparticles. *J Mater Chem A* 2015, **3**: 12550–12556.
[54] Duan YP, Liu Z, Jing H, *et al*. Novel microwave dielectric response of Ni/Co-doped manganese dioxides and their microwave absorbing properties. *J Mater Chem* 2012, **22**: 18291–18299.
[55] Ye F, Song Q, Zhang ZC, *et al*. Direct growth of edge-rich graphene with tunable dielectric properties in porous Si_3N_4 ceramic for broadband high-performance microwave absorption. *Adv Funct Mater* 2018, **28**: 1707205.
[56] Prodromakis T, Papavassiliou C. Engineering the Maxwell–Wagner polarization effect. *Appl Surf Sci* 2009, **255**: 6989–6994.

[57] O'Neill D, Bowman RM, Gregg JM. Dielectric enhancement and Maxwell–Wagner effects in ferroelectric superlattice structures. *Appl Phys Lett* 2000, **77**: 1520–1522.

[58] Wang NN, Wu F, Xie AM, *et al*. One-pot synthesis of biomass-derived carbonaceous spheres for excellent microwave absorption at the Ku band. *RSC Adv* 2015, **5**: 40531–40535.

[59] Fang PH. Cole–Cole diagram and the distribution of relaxation times. *J Chem Phys* 1965, **42**: 3411–3413.

[60] Wang P, Wang XM, Qiao L, *et al*. High-frequency magnetic properties and microwave absorption performance of oxidized Pr_2Co_{17} flakes/epoxy composite in X-band. *J Magn Magn Mater* 2018, **468**: 193–199.

[61] Duan YP, Guan HT. *Microwave Absorbing Materials*. New York: Jenny Stanford, 2016.

[62] Li YX, Wang JY, Liu RG, *et al*. Dependence of gigahertz microwave absorption on the mass fraction of Co@C nanocapsules in composite. *J Alloys Compd* 2017, **724**: 1023–1029.

[63] Zhao B, Zhao WY, Shao G, *et al*. Morphology-control synthesis of a core–shell structured NiCu alloy with tunable electromagnetic-wave absorption capabilities. *ACS Appl Mater Interfaces* 2015, **7**: 12951–12960.

[64] Meng FB, Zhao R, Zhan YQ, *et al*. Preparation and microwave absorption properties of Fe-phthalocyanine oligomer/Fe_3O_4 hybrid microspheres. *Appl Surf Sci* 2011, **257**: 5000–5006.

[65] Wu NN, Liu C, Xu DM, *et al*. Enhanced electromagnetic wave absorption of three-dimensional porous Fe_3O_4/C composite flowers. *ACS Sustainable Chem Eng* 2018, **6**: 12471–12480.

[66] Liu Y, Fu YW, Liu L, *et al*. Low-cost carbothermal reduction preparation of monodisperse Fe_3O_4/C core–shell nanosheets for improved microwave absorption. *ACS Appl Mater Interfaces* 2018, **10**: 16511–16520.

[67] Almasi-Kashi M, Mokarian MH, Alikhanzadeh-Arani S. Improvement of the microwave absorption properties in FeNi/PANI nanocomposites fabricated with different structures. *J Alloys Compd* 2018, **742**: 413–420.

[68] Su XL, Ning J, Jia Y, *et al*. Flower-like MoS_2 nanospheres: A promising material with good microwave absorption property in the frequency range of 8.2–12.4 GHz. *Nano* 2018, **13**: 1850084.

[69] Chen JH, Liu M, Yang T, *et al*. Improved microwave absorption performance of modified SiC in the 2–18 GHz frequency range. *CrystEngComm* 2017, **19**: 519–527.

[70] Farhan S, Wang RM, Li KZ. Electromagnetic interference shielding effectiveness of carbon foam containing *in situ* grown silicon carbide nanowires. *Ceram Int* 2016, **42**: 11330–11340.

[71] Han MK, Yin XW, Hou ZX, *et al*. Flexible and thermostable graphene/SiC nanowire foam composites with tunable electromagnetic wave absorption properties. *ACS Appl Mater Interfaces* 2017, **9**: 11803–11810.

[72] Jiang Y, Chen Y, Liu YJ, *et al*. Lightweight spongy bone-like graphene@SiC aerogel composites for high-performance microwave absorption. *Chem Eng J* 2018, **337**: 522–531.

[73] Kumar A, Agarwala V, Singh D. Effect of milling on dielectric and microwave absorption properties of SiC based composites. *Ceram Int* 2014, **40**: 1797–1806.

[74] Hu CG, Mou ZY, Lu GW, *et al*. 3D graphene–Fe_3O_4 nanocomposites with high-performance microwave absorption. *Phys Chem Chem Phys* 2013, **15**: 13038–13043.

[75] Wan YZ, Xiao J, Li CZ, *et al*. Microwave absorption properties of FeCo-coated carbon fibers with varying morphologies. *J Magn Magn Mater* 2016, **399**: 252–259.

[76] Zhang L, Zhu H, Song Y, *et al*. The electromagnetic characteristics and absorbing properties of multi-walled carbon nanotubes filled with Er_2O_3 nanoparticles as microwave absorbers. *Mater Sci Eng: B* 2008, **153**: 78–82.

[77] Zhao DL, Li X, Shen ZM. Preparation and electromagnetic and microwave absorbing properties of Fe-filled carbon nanotubes. *J Alloys Compd* 2009, **471**: 457–460.

[78] Zhu ZT, Sun X, Li GX, *et al*. Microwave-assisted synthesis of graphene–Ni composites with enhanced microwave absorption properties in Ku-band. *J Magn Magn Mater* 2015, **377**: 95–103.

[79] Green M, Tian LH, Xiang P, *et al*. FeP nanoparticles: A new material for microwave absorption. *Mater Chem Front* 2018, **2**: 1119–1125.

[80] Zhang WD, Zhang X, Wu HJ, *et al*. Impact of morphology and dielectric property on the microwave absorbing performance of MoS_2-based materials. *J Alloys Compd* 2018, **751**: 34–42.

[81] Liu PB, Huang Y, Zhang X. Cubic $NiFe_2O_4$ particles on graphene–polyaniline and their enhanced microwave absorption properties. *Compos Sci Technol* 2015, **107**: 54–60.

[82] She W, Bi H, Wen ZW, *et al*. Tunable microwave absorption frequency by aspect ratio of hollow polydopamine@α-MnO_2 microspindles studied by electron holography. *ACS Appl Mater Interfaces* 2016, **8**: 9782–9789.

[83] Yang HB, Ye T, Lin Y, *et al*. Excellent microwave absorption property of ternary composite: Polyaniline-$BaFe_{12}O_{19}$–$CoFe_2O_4$ powders. *J Alloys Compd* 2015, **653**: 135–139.

[84] Qing YC, Zhou WC, Luo F, *et al*. Optimization of electromagnetic matching of carbonyl iron/$BaTiO_3$ composites for microwave absorption. *J Magn Magn Mater* 2011, **323**: 600–606.

[85] Yang Y, Xu CL, Xia YX, *et al*. Synthesis and microwave absorption properties of FeCo nanoplates. *J Alloys Compd* 2010, **493**: 549–552.

[86] Ni SB, Sun XL, Wang XH, *et al*. Low temperature synthesis of Fe_3O_4 micro-spheres and its microwave absorption properties. *Mater Chem Phys* 2010, **124**: 353–358.

[87] Wu T, Liu Y, Zeng X, *et al*. Facile hydrothermal synthesis

of Fe_3O_4/C core–shell nanorings for efficient low-frequency microwave absorption. *ACS Appl Mater Interfaces* 2016, **8**: 7370–7380.

[88] Xiang Z, Song YM, Xiong J, *et al*. Enhanced electromagnetic wave absorption of nanoporous Fe_3O_4@carbon composites derived from metal-organic frameworks. *Carbon* 2019, **142**: 20–31.

[89] Zhao DL, Lv Q, Shen ZM. Fabrication and microwave absorbing properties of Ni–Zn spinel ferrites. *J Alloys Compd* 2009, **480**: 634–638.